Streamwise decay of localized states in channel flow

Stefan Zammert[1] and Bruno Eckhardt[2, 3]

[1] *Laboratory for Aero and Hydrodynamics, TU Delft, 2682 Delft, The Netherlands*
[2] *Fachbereich Physik, Philipps-Universität Marburg, D-35032 Marburg, Germany*
[3] *JM Burgerscentrum, TU Delft, 2682 Delft, The Netherlands*

(Dated: September 22, 2016)

Channel flow, the pressure driven flow between parallel plates, has exact coherent structures that show various degrees of localization. For states which are localized in streamwise direction but extended in spanwise direction, we show that they are exponentially localized, with decay constants that are different on the upstream and downstream side. We extend the analysis of Brand and Gibson, J. Fluid Mech. 750, R1 (2014), for stationary states to the case of advected structures that is needed here, and derive expressions for the decay in terms of eigenvalues and eigenfunctions of certain second order differential equations. The results are in very good agreement with observations on exact coherent structures of different transversal wave length.

PACS numbers:

arXiv:1609.06514v1 [physics.flu-dyn] 21 Sep 2016

Close to onset, turbulence in subcritical shear flows is spatially and temporally intermittent. One manifestation of the intermittency is the coexistence of laminar and turbulent regions for the same global flow conditions that result in chaotic spatio-temporal patterns [1–4]. Another is the existence of isolated localized turbulent structures which are not influenced by neighboring structures and can appear in the form of puffs or slugs in pipe flow [5] or spots in plane Couette [6–8] and Poiseuille flow [9]. The localized patterns and their evolution are important for an understanding of the spatio-temporal dynamics of transitional flows [10] and in particular for the proposed link to the phenomenology of directed percolation [11–13], where a sufficiently strong decay of the interactions between structures is one of the criteria for the selection of the appropriate universality class [14].

The relation between the transition to turbulence and exact coherent structures (ECS), their secondary bifurcations and the formation of a dense web of dynamical links between the different states has been studied in several flows [15–20]. For the case of plane Poiseuille flow (PPF) that is considered here, examples of ECS and their bifurcations include travelling waves [21–24], relative periodic orbits [25, 26] and streamwise [27] and doubly-localized relative periodic orbits [28].

For an understanding of localized turbulence from its microscale, localized ECS as described in [20, 23, 28–31] are necessary. The states tend to be exponentially localized in the streamwise direction, and more strongly localized in the spanwise direction. In very large domains, and if they are localized in both directions, there are indications for algebraic contributions as well. Specifically, localized ECS in plane Couette flow and plane Poiseuille flow show an exponential decay [23, 31] which for doubly-localized states becomes algebraic for large distances [28]. In pipe flow, the rate of decay in streamwise direction has been shown to decrease with increasing Reynolds number [32].

The model of Brand&Gibson [31] provides a rationale for an exponential decay and a relation between the decay, the Reynolds number, and the spanwise modulation in the case of plane Couette flow. It has been tested and verified for the streamwise velocity component in the tails of streamwise localized stationary solutions. We here extend their model to travelling ECS in plane Poiseuille flow, and show that the decay rates in the upstream and downstream direction are different, and that this asymmetry is controlled by the advection speed of the structures.

For our studies of PPF we choose a coordinate system where the x-axis is oriented along the direction of the flow and the plates are located parallel to the x-z-plane at $y = \pm d$. The Reynolds number $Re = U_0 d/\nu$ is defined using half the distance between the plates d together with the laminar center-line velocity U_0 and the kinematic viscosity ν. With U_0 and d the scales for velocity and length, the laminar profile becomes $U(y) = 1 - y^2$. We decompose the velocity field $\tilde{\mathbf{u}}$ into a laminar background and a deviation, $\tilde{\mathbf{u}} = U(y)\mathbf{e}_x + \mathbf{u}$, and will henceforth focus on the deviations $\mathbf{u} = (u, v, w)$, where u, v and w are the streamwise, wall-normal and spanwise velocity components, respectively.

For the numerical simulations we use the spectral code *Channelflow* [33], and for the identification of the exact solutions the Newton-method [34] already implemented in channelflow. For the linear algebra routines and the eigenvalue calculations we use the Eigen-package [35]. In all simulations, a constant mass flux is imposed. We use two states for the comparison between the theoretical predictions and the observed decay. One state, henceforth referred to as PO_E, is a streamwise localized ECS relative periodic orbit obtained by edge tracking [28, 36, 37]. The orbit is mirror-symmetric with respect to the center plane (s_y-symmetry). By restricting the system to a subspace symmetric under wall-normal (s_y) and spanwise (s_z) reflections, it is possible to identify a second streamwise localized relative periodic orbit, labelled PO_{Eyz}. Both states have in common that they are long-wavelength instabilities [32, 38] of streamwise extended travelling wave solutions: PO_E bifurcates sub-

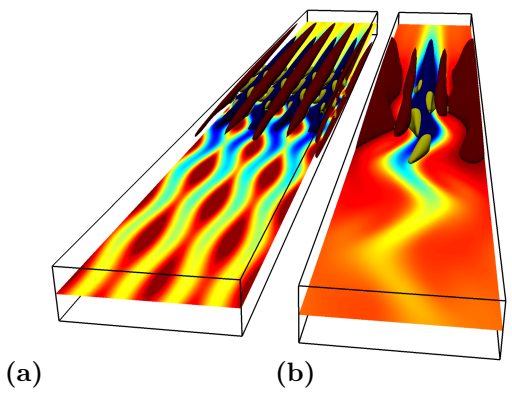

FIG. 1: Visualization of the two localized ECS PO_{Eyz} (a) and PO_E (b). The plots show isosurfaces of positive (red) and negative streamwise velocity and isosurfaces of the Q-vortex criterion (yellow) at $Q = 0.01$ and $Q = 0.001$. The entire computational domain is $402d$ long, but only a section of length $52d$ is shown in the figures. For both states the shown computational domain has width of 2π.

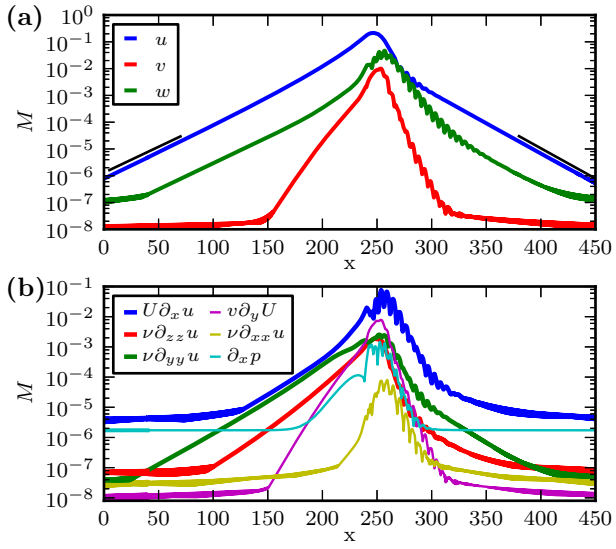

FIG. 2: Localization properties of the state PO_E at $Re = 1100$. (a) maximum M of the absolute values of the velocity components is shown versus streamwise coordinate x. Black lines show exponential decays with decays constants obtained from the model for the upstream and downstream tails. (b) the maximum norm of the terms of the linearized equations which contribute to the change of the streamwise component are shown.

critically from the travelling wave TW_E [28] and PO_{Eyz} connects at high Re to the travelling wave TW_{Eyz} [24]. The orbits are shown in Fig. 1. For the present study we prescribe spanwise wavenumbers of $\gamma = 1$ for PO_E and of $\gamma = 2$ for PO_{Eyz}. This allows us to study the dependence of the decay rates on the spanwise wavenumber, a parameter that affects the localization rate in plane Couette flow [31]. For the orbit PO_E a numerical resolution $N_y \times N_z = 49 \times 48$ with 24 modes per 2π length in streamwise direction is used. For PO_{Eyz} we use $N_y \times N_z = 49 \times 32$ and 32 modes per 2π in streamwise direction.

We quantify the localization properties using the maximum values of the velocity components as a function of streamwise coordinate x, with the maximum taken over spanwise and wall-normal positions, as shown in Fig. 2(a) for the state PO_E. As in previous studies [28, 31], all three velocity components decay exponentially, but since there is no symmetry in the flow direction, the decay rates in the upstream and downstream direction differ in general. One also notes that the decay of the streamwise and spanwise components are similar, but different from the one in the normal velocity component.

The key to the explanation of the decay rates is the observation that away from the center of the ECS, the velocity components are small and can be described with a linearization of the Navier-Stokes equation around the laminar profile. The terms that remain for the perturbation $\mathbf{u}$ are

$$\partial_t \mathbf{u} + U(y)\partial_x \mathbf{u} + v\partial_y U(y)\mathbf{e}_x = -\nabla p + \frac{1}{Re}\Delta \mathbf{u} \qquad (1)$$

Here, $U(y) = 1 - y^2$ is the laminar velocity profile and p the pressure fluctuations in the perturbation. In order to separate the contributions of each term to the equation, we show in Fig. 2(b) the maximum over spanwise and wall-normal positions of the different terms as a function of streamwise positions x. The data shows that in the tails we can neglect the coupling to the wall-normal velocity and to the base flow ($v\partial_y U$), as well as the second order derivative $\nu\partial_{xx}u$. We also neglect the pressure fluctuations since the plateau value which can be seen in Fig. 2(b) is related to the periodic boundary conditions and decreases with increasing domain length.

Without these terms, the equation for the streamwise component reduces to

$$\partial_t u + U(y)\partial_x u = Re^{-1}(\partial_{yy}u + \partial_{zz}u)\,. \qquad (2)$$

This equation is the plane Poiseuille flow equivalent of the equation obtained by Brand&Gibson [31] for the tails of localized states in plane Couette flow. It shows that the form of the equation is primarily a consequence of the cartesian geometry and of the linearization around the laminar profile.

The reflection symmetry on the midplane in plane Couette flow allows for the existence of stationary solutions, of the type analyzed in [31]. In the absence of this symmetry, all ECS for PPF are advected in streamwise direction. The travelling waves in plane Couette flow described in [39] also lack this symmetry and the analysis we describe here should also apply to localized versions of these travelling waves. Therefore, the ansatz for the flow field in the tails has to include the advection, and we take a spanwise periodic and streamwise travelling field of the form

$$u(x, y, z, t) = u(y)\exp\left[i\gamma z - \mu(x - ct)/Re\right]. \qquad (3)$$

In this ansatz γ is the spanwise wavenumber, c is the wave speed and μ is the decay rate that we want to calculate.

Substituting the ansatz and the PPF baseflow in Eq. 2 then gives

$$u'' - (\gamma^2 + \mu(c + y^2 - 1))u = 0 \tag{4}$$

and we have to seek solutions that satisfy the friction boundary conditions $u(\pm 1) = 0$. A general solution of this second order differential equation can be given in terms of parabolic cylinder functions $D_\nu(z)$ [40],

$$u(y) = a \cdot D_{\nu_1}(\sqrt{2}\sqrt[4]{\mu}y) + b \cdot D_{\nu_2}(i\sqrt{2}\sqrt[4]{\mu}y). \tag{5}$$

with indices $\nu_1 = (-\gamma^2 - c\mu + \mu - \sqrt{\mu})/(2\sqrt{\mu})$ and $\nu_2 = (\gamma^2 + (c-1)\mu - \sqrt{\mu})/(2\sqrt{\mu})$. The boundary conditions $u(\pm 1) = 0$ provide a set of linear equations that only has non-trivial solution if the discriminant

$$f(\mu) = D_{\nu_1}(-\sqrt{2}\sqrt[4]{\mu}) \cdot D_{\nu_2}(i\sqrt{2}\sqrt[4]{\mu}) - D_{\nu_1}(\sqrt{2}\sqrt[4]{\mu}) \cdot D_{\nu_2}(-i\sqrt{2}\sqrt[4]{\mu}). \tag{6}$$

vanishes. This function is readily evaluated using suitable numerical software, and one can compute or read off the zeros from curves like the ones shown in Fig. 3(a). The specific case in Fig. 3(a) uses the parameters $c = 0.85$ (the average wavespeed of PO_E at $Re = 1100$) and $\gamma = 1.0$, and has zeros at $\mu = -54.9$, -48.97 and 57.26.

However, the properties of the eigenvalues and the eigenfunctions become more transparent when considering the relation between (4) and an eigenvalue problem for a one-dimensional Schrödinger equation with a potential $V(y)$,

$$-u'' + V(y)u = Eu. \tag{7}$$

Eq. 4 is then reinterpreted as an eigenvalue problem for (7) with potential $V(y) = \gamma^2 + \mu(c-1) + \mu y^2$, boundary conditions $u(\pm 1) = 0$, and eigenvalue $E = 0$. Since γ and c are prescribed, the task is to determine μ such that the eigenvalue problem has a consistent solution. Examples of the potential and its eigenvalues are shown in Figs. 3(b) and (c). This form of the eigenvalue problem allows some qualitative conclusions and approximations to the decay rates and the shape of the profiles. As the type of the potential changes when μ changes sign, we consider the downstream and upstream situations separately.

On the downstream side, $\mu = \kappa^2$ is positive. Then the potential $V(y)$ is a harmonic oscillator with a minimum at $y = 0$ of depth $V_{min} = \gamma^2 + (c-1)\kappa^2$ and curvature $V'' = 2\kappa^2$. The minimum of the potential has to be negative, so that $c < 1$ and $\kappa^2 > \gamma^2/(1-c)$. The region where the potential is larger than the eigenvalue, $V(y) > 0$, is the classically forbidden region where the solutions usually fall off quickly. So if the boundary points $y = \pm 1$ are sufficiently far inside the forbidden region they may be moved out to $\pm\infty$ with little effect on the eigenvalues (and the eigenfunctions). For the case shown in Figs. 3(b) the forbidden region starts near $|x| \approx 0.4$ and

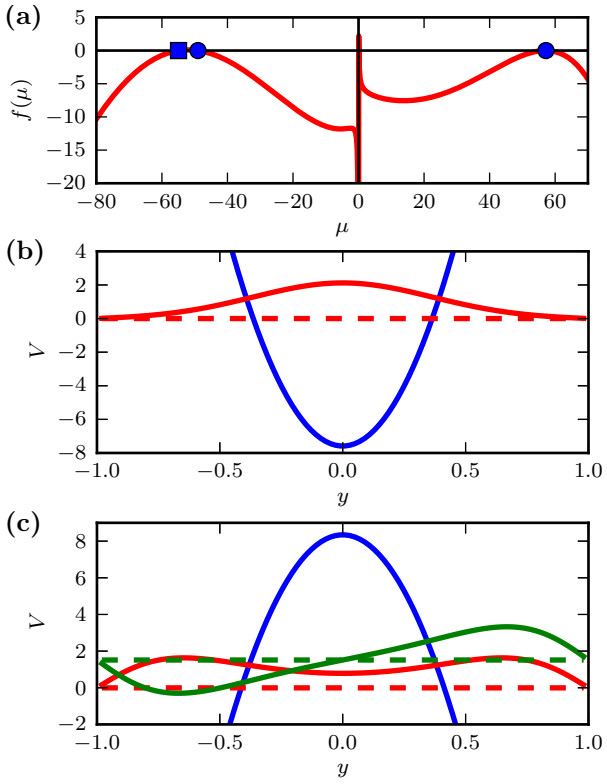

FIG. 3: Determination of the decay exponent μ. Panel (a) shows $f(\mu)$ vs. μ for $\gamma = 1.0$ and $c = 0.85$. The zeros are marked by blue symbols. Circles and squares are used if the corresponding profile is symmetric and asymmetric, respectively. At $\mu = 413$ (not shown) another zero with an asymmetric profile exists. Panel (b) shows the potential $V(y)$ for the downstream decay, for $\gamma = 1.0$, $c = 0.85$ and $\mu = 57.26$ (blue), where a symmetric eigenfunction with eigenvalue 0 exists (red). Panel (c) shows the potential for the parameters $\gamma = 1.0$, $c = 0.85$ and $\mu = -48.97$ (blue) on the upstream side. Here, 0 is an eigenvalue with a symmetric eigenfunction (red), while the asymmetric eigenfunction (green) corresponds to an eigenvalue of 1.51. The dashed lines in (b) and (c) indicate the positions of the eigenvalues for the eigenfunctions of the same color.

the approximation to consider the boundary conditions $u(\pm\infty) = 0$ is justified. The ground state for such a harmonic potential has a Gaussian form, $u \propto \exp(-\kappa y^2/2)$ and an eigenvalue that lies at a value κ above the minimum, so that the equation for κ becomes $V_{min} + \kappa = 0$ or

$$\gamma^2 - (1-c)\kappa^2 + \kappa = 0. \tag{8}$$

The relevant solution of this quadratic equation is

$$\kappa_0 = \frac{1}{2(1-c)} + \sqrt{\frac{\gamma^2}{1-c} + \frac{1}{4(1-c)^2}}. \tag{9}$$

For the specific case shown in Fig. 3, this results in the approximate values $\mu_0 \approx 57$, in excellent agreement with the value $\mu = 57.26$ from the exact expression. The calculation also shows that the eigenfunction can be well

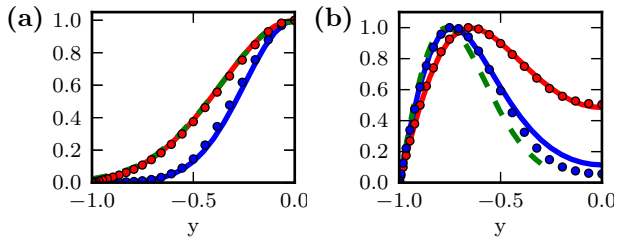

FIG. 4: Streamwise velocity profiles on the downstream (a) and upstream (b) side for the states PO_E (red) and PO_{Eyz} (blue) at $Re = 1100$ and $Re = 1800$, respectively. Circles represent DNS data and solid lines are used for the model profiles. In addition, the dashed green lines show a gaussian $\exp(-\kappa y^2/2)$ in (a), and an Airy function in (b), as approximate eigenfunctions for the corresponding eigenvalue problems for PO_E. Since the profiles are symmetric to the centerline, only one half of the channel width is shown.

approximated by a Gaussian controlled by $\kappa \approx 7.55$, as shown by the dashed green line in Fig. 4(a).

On the upstream side, μ is negative, and the potential is an inverted parabola with a maximum in the middle, $V_{max} = \gamma^2 + (1-c)|\mu|$. The potential assumes its minima at the walls, $V_{min} = \gamma^2 - |\mu|c$, and since these minima have to be negative, we have $|\mu| > \gamma^2/c$. The potential starts with a linear slope away from the wall, so that the approximate potential has the form $V \approx V_{min} + 2|\mu|\tilde{y}$, where $\tilde{y} = y + 1$ is the distance from the wall at $y = -1$. Proceeding as in the previous case one notes that the corresponding reference eigenvalue problem is that for eigenstates in a linear potential, with boundary conditions $u(0) = u(\infty) = 0$. This problem has Airy functions as its basic solutions, and a first eigenvalue at $E_1(2|\mu|)^{2/3}$ above the potential minimum, where $E_1 = 2.338$ is the numerical value in a potential with slope 1, [41]. Accordingly, the determining equation for μ becomes

$$\gamma^2 - |\mu|c + E_1(2|\mu|)^{2/3} = 0, \qquad (10)$$

with the approximate solution $|\mu| \approx (4.676/c)^3(1 + 0.029c^2\gamma^2)$. For TW_E at $Re = 1100$ the decay rate from the approximate model becomes $\mu = -86$, which differs considerably from the value obtained from the exact equation. The reason for this discrepancy is apparent from the form of the potential: the classically forbidden region lies in the center, but the value of the potential is not very high, so that the profile still maintains a significant value near 0 before it enters the other boundary layer. The approximate expression for the eigenvalues shows, however, that this situation will change when the structures are closer to the wall where the wave speed c becomes smaller and the damping $|\mu|$ stronger. Similarly, also larger values of γ will give stronger localization near the wall and along the streamwise direction.

In order to compare the predictions for the decay from the model (2-6) to the DNS data for the two states PO_E and PO_{Eyz} we have to extract decay rates from the DNS data. For the decay constants we fit an exponential to the spanwise wall-normal maximum of the streamwise velocity component on the downstream and upstream sides of the structures. To avoid congestion by transients, we only use data that are at least $100d$ (upstream side) and $50d$ (downstream side) from the center of the structures. The domains used in the simulations are therefore necessarily very long. For the orbit PO_E the decay constants were calculated in a domain with a streamwise length L_x of $565h$. For shorter domains decay rates that are smaller in absolute value, corresponding to a slower decay, are observed. The rates for the tails of the two structures and for different Reynolds numbers are shown in Figs. 5(a) and (b) using solid symbols.

The spanwise wavenumber γ that enters the model represents the wavenumbers in the structures that dominate the tails, and does not need to coincide with the wavenumber of the domain. We therefore compared the observed decay with decays computed from (6) for different values of γ. For PO_E we find that the best fit is achieved for $\gamma = 1$, the wavenumber of the domain. For the mirror symmetric state PO_{Eyz} the best agreement with the numerical data is achieved for $\gamma = 4$, twice the value of the domain size. This decrease in wavelength in the tail is induced by the spanwise mirror symmetry of the structure and reflected in the presence of four streaks in Fig. 1(a)

The ansatz for the velocity field in (3) describes the decay in downstream direction as $\exp(-\mu x/Re)$, and suggests that both the upstream and downstream length of the structures should increase proportional to Re. However, the eigenvalue problem (4) for μ contains an implicit Re dependence due to the variation of the wave speed $c(Re)$. As shown in Fig. 5(c), the wave speed c, determined as the average wave speed of an ECS calculated by dividing the displacement over one period by the length of the period, increases with Reynolds number. It is only once this dependence is taken into account that the localization rates determined from the DNS and from the model give the very good agreement shown in Figs. 5(a) and (b). The model data are also shown in Fig. 2(a) where a black line indicates the theoretical prediction for the streamwise component (blue). The effects of the Reynolds number dependence on the localization length of the structures are different on the upstream and downstream side. On the upstream side, Fig. 5(a) shows that μ becomes less negative with increasing Re. Accordingly, the localization length, defined as $Re/|\mu|$, increases with Re and the structures become stretched out along the wall. On the downstream side, Fig. 5(b) shows that $\mu(Re)$ increases, roughly proportional to Re, so that the localization length $Re/|\mu|$ varies only little. This is in agreement with observations in [28]. The localization properties of modes with different spanwise wavenumbers γ are shown in Fig. 6. The increasing absolute value $|\mu|$ on the upstream side indicates more strongly localized structures, whereas there are little changes on the downstream side. The wave speeds used in Fig. 6 are near 1/2. In the limit $c \to 1$, which may be obtained for structures

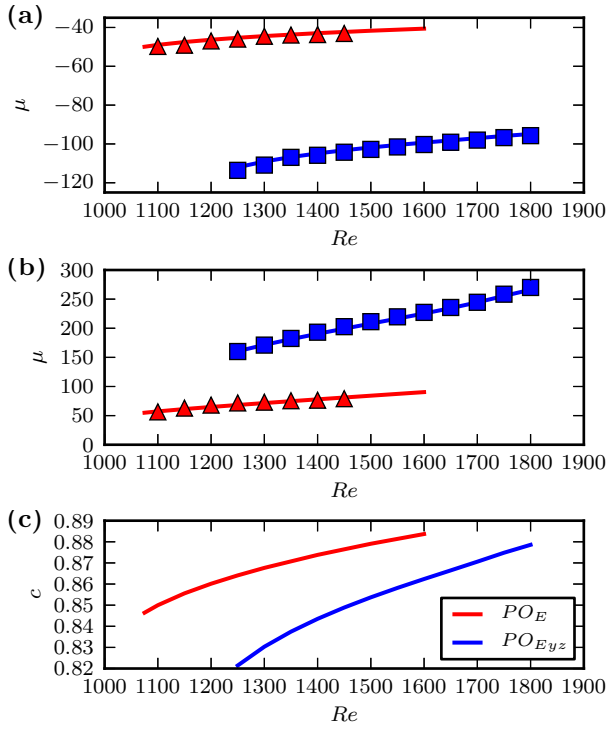

FIG. 5: Decay constants for exact coherent states as a function of Reynolds number. (a) upstream side for PO_E (red) and PO_{Eyz} (blue). The model predictions, which are obtained from roots of Eq. 6, are shown as continuous lines, the decay rates fitted to the DNS data as triangles and squares, respectively. (b) same as (a) for the downstream side. (c) average wavespeed for both states. The variation in wavespeed with Re is responsible for the variation in decay constants.

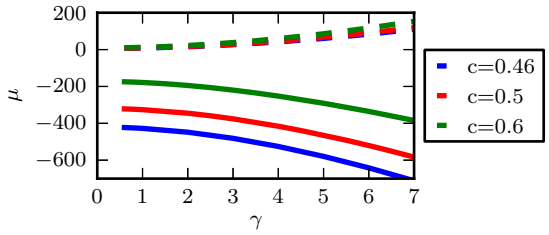

FIG. 6: Dependence of the decay constants μ on the spanwise wavenumber γ for different wavespeeds c for the symmetric profile on the upstream (solid) and downstream side (dashed).

that are localized in the center, and in the limit $c \to 0$ for structures that are localized very close to the walls, the eigenvalues diverge and the structures should become strongly localized (in the downstream and upstream direction, respectively). However, we do not have examples of flow structures on which to verify this prediction.

The present extension of the Brand&Gibson [31] analysis to advective structures in PPF shows how the decay and the profile of the structures on the downstream and upstream side are related to the wave speed and spanwise wavenumber. Similar analyses should be possible for other advected structures, such as localized version of travelling waves in plane Couette flow [39] or localized structures in the asymptotic suction boundary layer [42].

This work was supported in part by the DFG within FOR 1182 and by Stichting voor Fundamenteel Onderzoek der Materie (FOM) within the program “Towards ultimate turbulence”.

[1] D. Barkley and L. Tuckerman, Phys. Rev. Lett. **94**, 014502 (2005).
[2] G. Brethouwer, Y. Duguet, and P. Schlatter, J. Fluid Mech. **704**, 137 (2012).
[3] M. Avila and B. Hof, Phys. Rev. E **87**, 063012 (2013).
[4] D. Moxey and D. Barkley, Proc. Natl. Acad. Sci. U. S. A. **107**, 8091 (2010).
[5] I. Wygnanski, M. Sokolov, and D. Friedman, J. Fluid Mech. **69**, 283 (1975).
[6] D. R. Carlson, S. E. Widnall, and M. F. Peeters, J. Fluid Mech. **121**, 487 (1982).
[7] A. Lundbladh and A. V. Johansson, J. Fluid Mech. **229**, 499 (1991).
[8] J. Schumacher and B. Eckhardt, Phys. Rev. E **63**, 046307 (2001).
[9] G. Lemoult, K. Gumowski, J.-L. Aider, and J. E. Wesfreid, Eur. Phys. J. E **37** (2014).
[10] B. Eckhardt, J. Fluid Mech. **758**, 1 (2014).
[11] G. Lemoult, L. Shi, K. Avila, S. V. Jalikop, M. Avila, and B. Hof, Nat. Phys. **12**, 254 (2016).
[12] M. Sano and K. Tamai, Nat. Phys. **12**, 249 (2015).
[13] K. T. Allhoff and B. Eckhardt, Fluid Dyn. Res. **44**, 031201 (2012).
[14] H. Hinrichsen, Adv. Phys. **49**, 815 (2000).
[15] A. Schmiegel, Phd thesis, Philipps-Universitität Marburg (1999), URL `http://archiv.ub.uni-marburg.de/diss/z2000/0062/pdf/z2000-0062.pdf`.
[16] J. F. Gibson, J. Halcrow, and P. Cvitanović, J. Fluid Mech. **638**, 243 (2009).
[17] G. Kawahara, M. Uhlmann, and L. van Veen, Annu. Rev. Fluid Mech. **44**, 203 (2012).
[18] F. Mellibovsky and B. Eckhardt, J. Fluid Mech. **709**, 149 (2012).
[19] T. Kreilos and B. Eckhardt, Chaos **22**, 047505 (2012).
[20] M. Avila, F. Mellibovsky, N. Roland, and B. Hof, Phys. Rev. Lett. **110**, 224502 (2013).
[21] M. Nagata and K. Deguchi, J. Fluid Mech **735**, R4 (2013).
[22] D. P. Wall and M. Nagata, J. Fluid Mech. **788**, 444 (2016).
[23] J. F. Gibson and E. Brand, J. Fluid Mech. **745**, 25 (2014).
[24] S. Zammert and B. Eckhardt, Phys. Rev. E **91**, 041003(R) (2015).
[25] S. Toh and T. Itano, J. Fluid Mech. **481**, 67 (2003).
[26] S. Zammert and B. Eckhardt, Fluid Dyn. Res. **46**, 041419 (2014).
[27] F. Mellibovsky and A. Meseguer, J. Fluid Mech. **779**, R1

(2015).
[28] S. Zammert and B. Eckhardt, J. Fluid Mech. **761**, 348 (2014).
[29] T. M. Schneider, J. F. Gibson, and J. Burke, Phys. Rev. Lett. **104**, 104501 (2010).
[30] T. M. Schneider, D. Marinc, and B. Eckhardt, J. Fluid Mech. **646**, 441 (2010).
[31] E. Brand and J. F. Gibson, J. Fluid Mech. **750**, R1 (2014).
[32] M. Chantry, A. P. Willis, and R. R. Kerswell, Phys. Rev. Lett. **112**, 164501 (2014).
[33] J. F. Gibson, Tech. Rep., U. New Hampshire (2012), URL `Channelflow.org`.
[34] D. Viswanath, J. Fluid Mech. **580**, 339 (2007).
[35] G. Guennebaud, B. Jacon, and Others, *Eigen v3* (2010), URL `http://eigen.tuxfamily.org`.
[36] J. Skufca, J. A. Yorke, and B. Eckhardt, Phys. Rev. Lett. **96**, 174101 (2006).
[37] T. M. Schneider, B. Eckhardt, and J. Yorke, Phys. Rev. Lett. **99**, 034502 (2007).
[38] K. Melnikov, T. Kreilos, and B. Eckhardt, Phys. Rev. E **89**, 043008 (2014).
[39] M. Nagata, Phys. Rev. E **55**, 2023 (1997).
[40] I. S. Gradshteyn and I. M. Ryzhik, *Table of Integrals, Series, and Products* (Academic Press, 2007), 7th ed.
[41] S. Flügge, *Practical Quantum Mechanics* (Springer, Berlin/Heidelberg, 1999).
[42] T. Khapko, T. Kreilos, P. Schlatter, Y. Duguet, B. Eckhardt, and D. S. Henningson Phys. Rev. Fluids **1**, 043602 (2016).